

Self-Templated Formation of P2-type $\text{K}_{0.6}\text{CoO}_2$ Microspheres for High Reversible Potassium-Ion Batteries

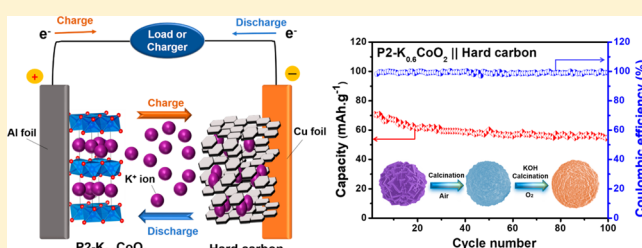
Tao Deng,[†] Xiulin Fan,[†] Chao Luo,[†] Ji Chen,^{†,‡} Long Chen,[†] Singyuk Hou,[†] Nico Eidson,[†] Xiuquan Zhou,^{‡,§} and Chunsheng Wang^{*,†,§}

[†]Department of Chemical and Biomolecular Engineering and [‡]Department of Chemistry and Biochemistry, University of Maryland, College Park, Maryland 20742, United States

Supporting Information

ABSTRACT: Layered metal oxides have been widely used as the best cathode materials for commercial lithium-ion batteries and are being intensively explored for sodium-ion batteries. However, their application to potassium-ion batteries (PIBs) is hampered because of the poor cycling stability and low rate capability due to the larger ionic size of K^+ than of Li^+ or Na^+ . Herein, a facile self-templated strategy was used to synthesize unique P2-type $\text{K}_{0.6}\text{CoO}_2$ microspheres that consist of aggregated primary nanoplates as PIB cathodes. The unique $\text{K}_{0.6}\text{CoO}_2$ microspheres with aggregated structure significantly enhanced the kinetics of the K^+ intercalation/deintercalation and also minimized the parasitic reactions between the electrolyte and $\text{K}_{0.6}\text{CoO}_2$. The P2- $\text{K}_{0.6}\text{CoO}_2$ microspheres demonstrated a high reversible capacity of 82 mAh g^{-1} at 10 mA g^{-1} , high rate capability of 65 mAh g^{-1} at 100 mA g^{-1} , and long cycle life (87% capacity retention over 300 cycles). The high reversibility of the P2- $\text{K}_{0.6}\text{CoO}_2$ full cell paired with a hard carbon anode further demonstrated the feasibility of PIBs. This work not only successfully demonstrates exceptional performance of P2-type $\text{K}_{0.6}\text{CoO}_2$ cathodes and microspheres $\text{K}_{0.6}\text{CoO}_2$ ||hard carbon full cells, but also provides new insights into the exploration of other layered metal oxides for PIBs.

KEYWORDS: Cathode material, layered metal oxides, $\text{K}_{0.6}\text{CoO}_2$, high reversibility, potassium-ion battery



As demand for mobile devices rapidly increases, lithium-ion batteries (LIBs) have become the most widely used energy storage medium, due to high working voltage, large energy density, and long cycle life.^{1–3} Recently, LIBs are expanding their commercial application from portable electronics to electric vehicles, which raises concerns on the availability and rising price of lithium resources.^{4–6} On the other hand, the growing renewable energy storage market from wind, solar, hydropower, and other sources has led to an urgent need of reliable and more cost-effective alternatives for expensive LIBs. Such situation has spurred considerable research on Na-ion based systems.^{5,7–14} Compared with LIBs, sodium-ion batteries (SIBs) are always restricted by the less negative redox potential, resulting in lower energy density and higher operating cost.^{15–17} Recently, potassium-ion batteries (PIBs) were proposed and regarded as a one of the most promising alternatives to LIBs because K has a high natural abundance, lower standard redox potential than Na ($\text{Li}/\text{Li}^+ = -3.040 \text{ V}$; $\text{K}/\text{K}^+ = -2.936 \text{ V}$; $\text{Na}/\text{Na}^+ = -2.714 \text{ V}$ vs SHE), as well as property similarities to Li.^{17–19} A detailed comparison of Li, Na, and K as ionic carriers in nonaqueous rechargeable batteries is summarized in Table S1.

Extensive efforts were made to explore suitable electrode materials with low cost, large capacity, and long cycle life for PIBs.^{15,18,20–31} Unlike SIBs that are limited by the lack of suitable anode materials, PIBs are able to utilize graphite as an

anode material.^{16,19,24,26–30,32–35} In addition to graphite, soft and hard carbon are also promising anode candidates, because they can provide not only high capacity but better rate performance and cycle life.^{24,33,36} While PIBs have an advantage on the anode side, the situation is different for the cathode. Only a few cathode compounds have been reported for PIBs due to much more stringent intercalation requirements caused by the larger ionic size and mass of K^+ . Among all the reported cathode materials, Prussian blue (PB) was the first reported cathode material that could reversibly store K-ions in nonaqueous electrolytes with long cycle life.^{18,19} Although there have been extensive studies on PB and PB-related family compounds, the low volumetric capacity due to the low density of hexacyanoferrates limits their practical applications.^{19,21,22,37–40} In contrast, layered metal oxides that have been widely used as LIB and SIB cathodes can potentially achieve both high volumetric and gravimetric energy density for PIBs. Vaalma et al. demonstrated that layered $\text{K}_{0.3}\text{MnO}_2$ can work as PIB cathodes.³⁶ $\text{K}_{0.7}\text{Fe}_{0.5}\text{Mn}_{0.5}\text{O}_2$ nanowires showed even better performance as a cathode for PIBs.³¹ The K-ion intercalation/deintercalation mechanism of layered $\text{K}_{0.5}\text{MnO}_2$ and $\text{K}_{0.6}\text{CoO}_2$ was also reported by Ceder et al.^{15,30} However, the electrochemical performance of these layered metal oxide

Received: December 19, 2017

Published: January 2, 2018

cathodes in PIBs is far worse than in LIBs and SIBs due to large structure changes and distortions when K-ions intercalate and deintercalate.³⁸ Severe side reactions with the electrolyte is another major concern with layered metal oxide cathodes in PIBs.^{19,38} These challenges require layered metal oxide particles to be microsized in order to reduce the side reactions but still need to be assembled by nano- or submicron primary particles to facilitate K-ion reaction kinetics.

Such micron-sized hierarchical structured spheres assembled from the nano- or submicron primary particles have been applied to LIB and SIB cathodes,⁴¹ showing exceptional electrochemical performance. The nanosized primary particles can ensure the fast ion intercalation/deintercalation, while the microsized spheres can minimize the parasitic reactions and improve the volumetric energy densities of the battery.^{15,42–44} Because of the larger ionic size of K-ion⁴⁵ and prone side reactions between the electrode and the electrolyte,^{19,46} the synergetic effect of the hierarchical structure should be more pronounced on PIBs.

Herein, we synthesized P2-type layered $K_{0.6}CoO_2$ microspheres that are composed of nano- and submicron plates as primary particles through a two-step self-templating method. The uniform $K_{0.6}CoO_2$ microspheres presented excellent electrochemical performance toward K storage with a high overall capacity, fast K^+ intercalation/deintercalation capability, and high reversibility. Specifically, the uniform P2-type $K_{0.6}CoO_2$ microspheres delivered a high capacity of 82 mA h g^{-1} at 10 mA g^{-1} and maintained a high capacity of 65 mA h g^{-1} at 40 mA g^{-1} for over 300 cycles with an extremely low capacity decay rate of <0.04% per cycle, which is approximately 5 times lower than the capacity decay rate of layered metal oxides cathodes made by solid state methods in PIBs.^{15,30,36,46} In addition, a full cell composed of a P2-type $K_{0.6}CoO_2$ microsphere cathode and hard carbon anode delivered a high discharge capacity of 71 mA h g^{-1} at a current density of 30 mA h g^{-1} with a high capacity retention of >80% after 100 cycles.

Overall strategy for the synthesis of P2-type $K_{0.6}CoO_2$ microspheres is schematically depicted in Figure 1. Briefly,

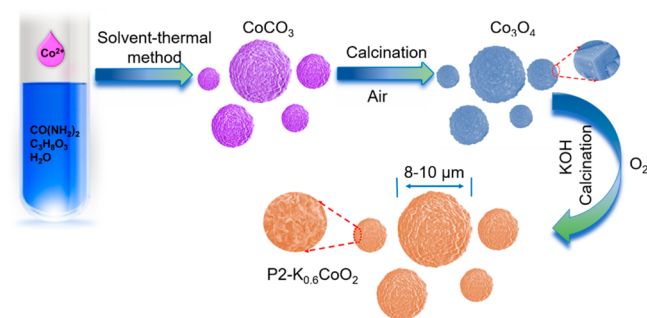


Figure 1. Schematic illustration for the synthesis of uniform P2-type $K_{0.6}CoO_2$ microspheres.

$CoCO_3$ microspheres consisting of uniform cubic primary particles were prepared by a modified solvent-thermal treatment of $CoCl_2 \cdot 6H_2O$ in glycerol–urea mixed solution at 180 °C. During the solvent-thermal synthesis, $CoCl_2 \cdot 6H_2O$ crystals were reconstructed in the presence of glycerol and resulted in the formation of uniform $CoCO_3$ microspheres. The $CoCO_3$ microspheres were calcined into Co_3O_4 microspheres in air, which present porous structures due to the release of CO_2 at high temperature. The prepared porous Co_3O_4 microspheres

reacted with KOH at elevated temperature to produce the P2-type $K_{0.6}CoO_2$ microspheres. A more detailed description about the synthesis process, called two-step self-templating method, is given in the Supporting Information. Compared with the classical solid-state calcination method¹⁵ (see Supporting Information), the P2-type $K_{0.6}CoO_2$ microparticles maintained the spherical morphology of $CoCO_3$, although at a high calcination temperature. The P2- $K_{0.6}CoO_2$ microspheres should simultaneously resolve the aforementioned challenges of KIB cathodes by making use of the $CoCO_3$ microsize and uniform hierarchical structure.

The as-synthesized cathode materials for PIBs were characterized by X-ray diffraction (XRD), scanning electron microscopy (SEM), and transmission electron microscopy (TEM). Figure 2 shows the Rietveld-refined profile of the XRD

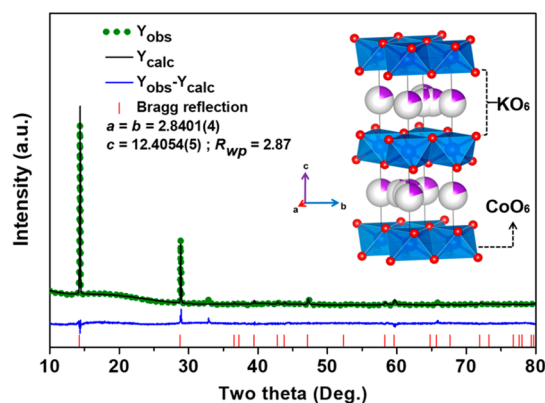


Figure 2. Rietveld refinement of X-ray diffraction data and schematic structure of the P2-type $K_{0.6}CoO_2$ microspheres.

pattern of a typical $K_{0.6}CoO_2$ sample. The unusual background between 10° and 30° arises from amorphous scattering caused by the Kapton film used to seal the sample during XRD characterization. The structure was fit to the $P6_3/mmc$ space group and the lattice parameters were determined as $a = b = 2.8401(4)$ Å and $c = 12.4054(5)$ Å, which is consistent with previous literature.^{15,47} On the basis of the aforementioned structural analysis, the $K_{0.6}CoO_2$ has a P2-type layered hexagonal structure (the inset of Figure 2), consisting of hexagonal close-packed oxygen with K atoms in the interstitial sites while Co atoms occupy the octahedral sites.¹³ The results from inductively coupled plasma optical emission spectroscopy (ICP-OES) analysis further confirmed the ratio of K and Co is $\approx 0.58:1.0$. Compared with Li and Na, 1.0 and 0.74 in Li_xCoO_2 , and Na_xCoO_2 respectively, the smaller value of ~ 0.6 for K in the K_xCoO_2 materials originates from the larger size of K-ions that occupy less sites in layered structures. The larger K-ion size causes larger repulsion forces, leading to increased lattice parameters.¹⁵

Figure 3 shows the morphology and structure of the $CoCO_3$ precursor, the Co_3O_4 intermediate, and the final P2-type $K_{0.6}CoO_2$ microspheres. The insets are the optical images of the corresponding powders. As shown in Figure 3a, the purple $CoCO_3$ precursors present as uniform microspheres with diameters of 8–10 μm . Figure 3b shows the enlarged SEM image of $CoCO_3$ microspheres, in which ideal cubes protruded out from the spheres. After annealing in air, the purple $CoCO_3$ precursors were transformed to black Co_3O_4 microspheres. These Co_3O_4 microspheres exhibit the same size and spherical morphology as $CoCO_3$, while many of the pores with sizes of

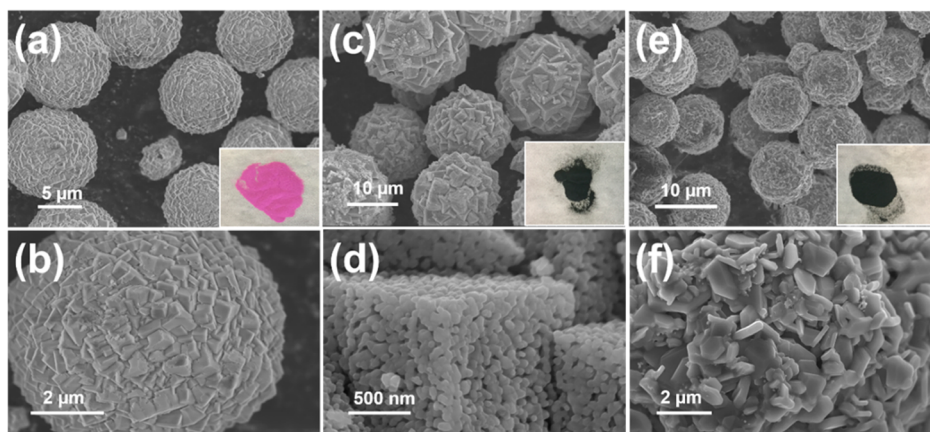


Figure 3. SEM images of as-synthesized (a,b) CoCO_3 precursor microspheres, (c,d) Co_3O_4 intermediate microspheres, and (e,f) P2-type $\text{K}_{0.6}\text{CoO}_2$ microspheres; insets are the corresponding prepared samples for characterization.

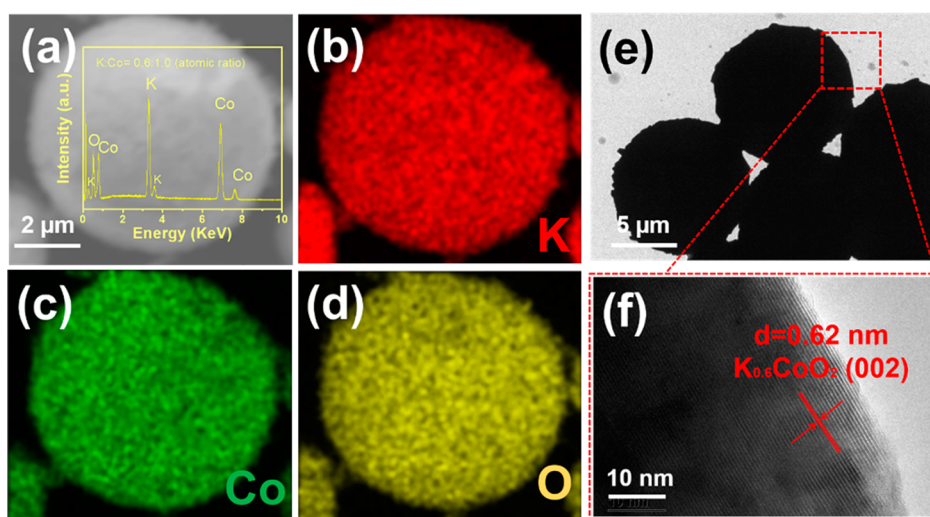


Figure 4. (a) Typical SEM images of P2-type $\text{K}_{0.6}\text{CoO}_2$ microspheres and corresponding elemental mapping of (b) potassium, (c) cobalt, and (d) oxygen elements. (e,f) Different magnification HRTEM images of P2-type $\text{K}_{0.6}\text{CoO}_2$ microspheres.

~ 10 nm show up in the primary cubic particles due to the release of CO_2 during annealing (Figure 3c,d). Figure 3e,f presents the final phase-pure K_xCoO_2 microspheres with high crystallinity, demonstrating that the second calcination at an elevated temperature did not destroy the spherical structure. Obviously, the surface morphology of P2-type $\text{K}_{0.6}\text{CoO}_2$ is different from that of CoCO_3 precursor and Co_3O_4 intermediate microspheres, which is caused by the recrystallization and crystal growth at high temperature. These uniform, submicron-sized flakes could improve the K-ion intercalation/deintercalation kinetics compared with the bulk materials because of the shortened migration distances and more intercalation/deintercalation sites. In addition, the average size of CoCO_3 precursor microspheres increased from $10 \mu\text{m}$ to about $20 \mu\text{m}$ during first calcination at 500°C but returned to $8\text{--}10 \mu\text{m}$ for final P2- $\text{K}_{0.6}\text{CoO}_2$ after the second calcination with KOH. As a result, the measured tap density of s-KCO (1.96 g cm^{-3}) is higher than those of mesoporous Co_3O_4 (1.2 g cm^{-3}) and i-KCO (1.6 g cm^{-3}).

To understand the effect of this hierarchical structure on the electrochemical performance, a typical P2-type $\text{K}_{0.6}\text{CoO}_2$ sample with irregular morphology was synthesized using a traditional solid-state method and evaluated as the cathode

material for PIBs. The detailed synthesis procedures can be found in the experimental section given in the Supporting Information. For convenience, the spherical P2-type $\text{K}_{0.6}\text{CoO}_2$ and irregular P2-type $\text{K}_{0.6}\text{CoO}_2$ is denoted as s-KCO and i-KCO, respectively. As showed in Figure S1, i-KCO has an irregular shape with an average particle size of around $20 \mu\text{m}$, which is much larger than that of s-KCO. The uniform composition and elemental distribution of s-KCO were confirmed by energy dispersive X-ray spectroscopy (EDS), as shown in Figure 4a–d. The K, Co, and O elements are uniformly distributed in all s-KCO microspheres, demonstrating that the two-step synthesis is very effective in synthesizing compounds with complex hierarchical structures. Also, a K/Co atomic ratio of ~ 0.6 further confirms the chemical composition of P2-type $\text{K}_{0.6}\text{CoO}_2$. In addition, high-resolution transmission electron microscopy (HRTEM) of s-KCO in Figure 4e,f reveals lattice fringes with a spacing of 0.62 nm which matches well with the (002) planes of $\text{K}_{0.6}\text{CoO}_2$ (hexagonal, $P6_3/mmc$). The distinct lattice fringes on the microspheres clearly show that as-obtained s-KCO has a well-defined crystal structure.

The electrochemical performance of s-KCO and i-KCO was investigated using cyclic voltammetry (CV) and galvanostatic charge/discharge cycling in a half-cell configuration. Figure 5a

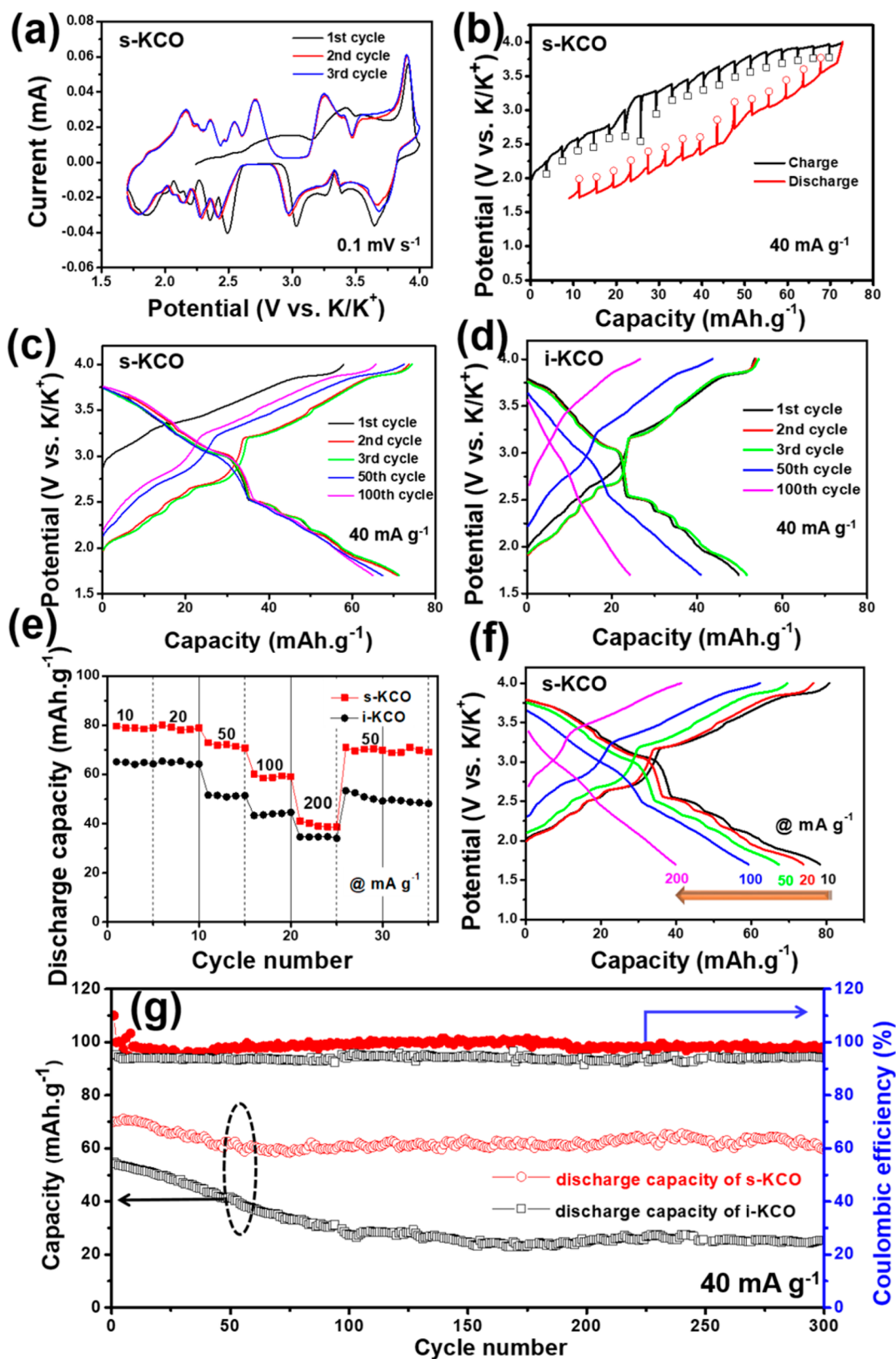


Figure 5. Electrochemical performance of s-KCO and i-KCO in $K_xCoO_2||K$ half-cell configuration. (a) CV curves for the s-KCO electrode at a scanning rate of 0.1 mV s^{-1} . (b) Potential response of s-KCO during GITT measurement at a constant current of 40 mA g^{-1} , the hollow dots represent the equilibrium OCP. (c,d) Electrochemical charge/discharge curves of s-KCO and i-KCO at a constant current of 40 mA g^{-1} . (e) Rate capability of s-KCO and i-KCO at different current rates, increasing from 10 mA g^{-1} to 200 mA g^{-1} . (f) Potential-capacity curves of s-KCO at different current densities, increasing from 10 mA g^{-1} to 200 mA g^{-1} . (g) Cycling performance of s-KCO and i-KCO at a constant current of 40 mA g^{-1} . All of the current densities and capacities were calculated based on the weight of active material K_xCoO_2 . All the tests were performed in the voltage range of 1.7–4.0 V (vs K/K⁺) at room temperature.

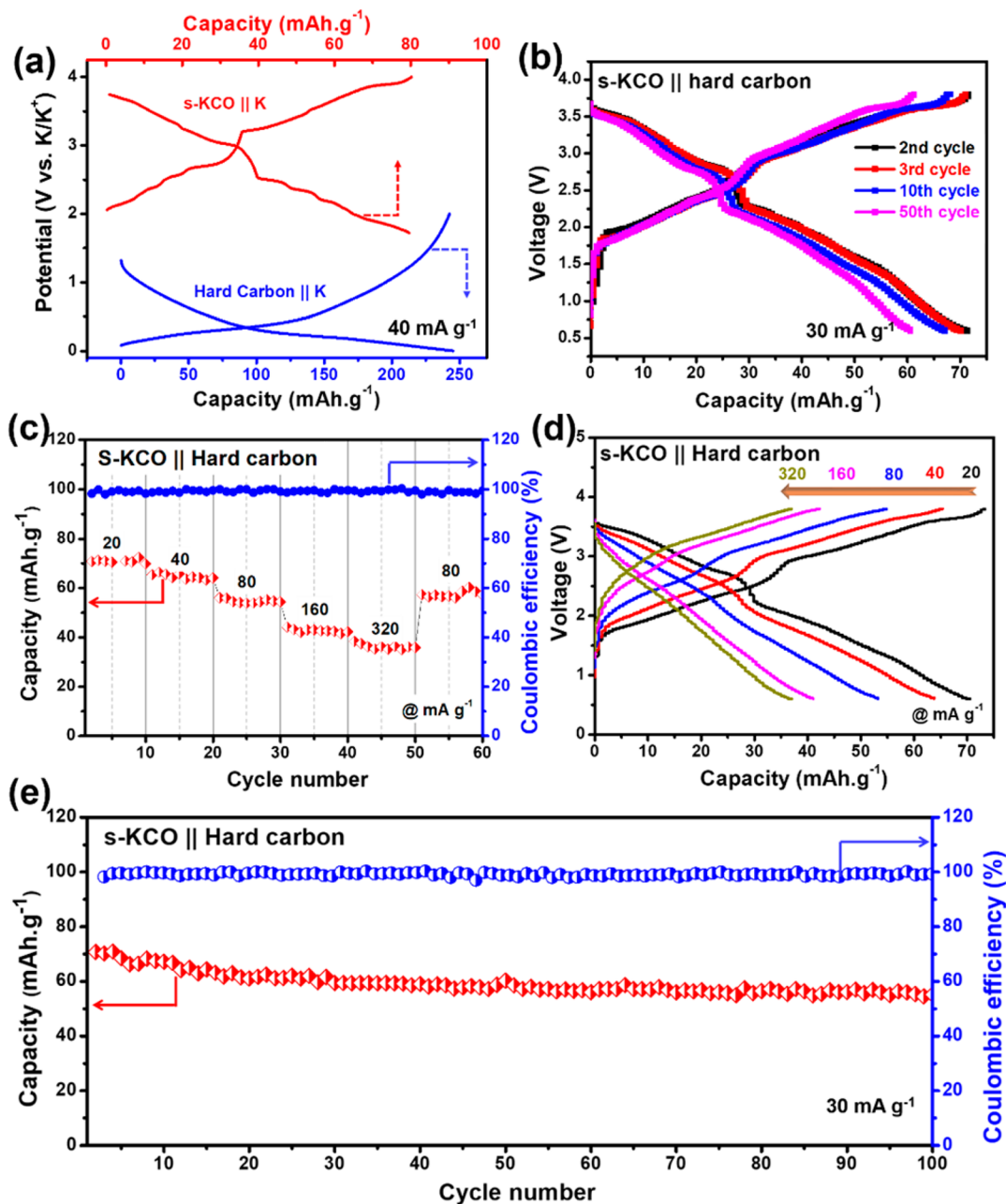


Figure 6. Demonstration of PIBs based on s-KCO||hard carbon configuration. (a) Typical charge–discharge curves of s-KCO||K and hard carbon||K in a half-cell configuration. (b) Electrochemical charge–discharge voltage profiles of PIBs, cycled at a current rate of 30 mA g⁻¹. (c) Rate capability of PIBs at different current rates, increasing from 20 to 320 mA g⁻¹. (d) Voltage–capacity curves of PIBs at different current densities, increasing from 20 to 320 mA g⁻¹. (e) Cycling performance of PIBs at a constant current of 30 mA g⁻¹. All the current densities were normalized by the weight of active material on the cathode side. All the tests for full cell were performed in the voltage range of 0.5–3.8 V at room temperature.

shows the first three CV curves of an s-KCO cathode in the voltage range of 1.7–4.0 V (vs K/K⁺) at a scanning rate of 0.1 mV/s. Obviously, the s-KCO cathode presents multiple pairs of redox peaks, which is caused by complex phase transition reactions during K-ion intercalation/deintercalation.^{15,38} Similar to other P2-type oxides cathode materials of PIBs, the complicated phase transition is mainly due to the changeable states of K⁺/vacancy ordering and CoO₂ layer gliding during K-ion intercalation/deintercalation.^{11,13,41} The overlap of the CV profiles after the first cycle also indicates the excellent reversibility for the s-KCO electrode during potassiation/depotassiation cycling.

The thermodynamic potential hysteresis, as well as kinetic overpotentials of s-KCO at different potassiation/depotassiation levels, was further investigated using galvanostatic intermittent titration technique (GITT) after the fifth cycle activation process. The GITT measurement was conducted with a pulse current of 40 mA g⁻¹ for a duration time of 5 min, followed by a long relaxation of 2 h at open circuit to obtain the quasi-equilibrium potential. Figure 5b presents the potential response during the GITT measurement for the s-KCO electrode, where the quasi-equilibrium open-circuit potential (OCP) is highlighted by hollow dots in the curve. The complete profile for the potassiation/depotassiation process along with the potential relaxation during the open circuit

periods has been provided in Figure S2. As shown in Figure 5b, the quasi-thermodynamic potential hysteresis of s-KCO in each current pulse is in the range of 0.15–0.20 V for both charge and discharge curves, which indicates a large kinetic overpotential existing in K^+ intercalation/deintercalation process due to the large ionic size of K-ion. The unusual large overpotential (~ 0.6 V) at 2.5 and 2.8 V is mainly attributed to the large potential drop caused by phase transformation, which corresponds to $x = 0.5$ for K_xCoO_2 in Figure S3. The large overpotentials suggest that ion diffusion and phase transformation control the reaction kinetics of s-KCO.

Figure 5c,d shows the potential profiles of s-KCO and i-KCO electrodes at a current density of 40 mA g^{-1} between 1.7 and 4.0 V (vs K/K). The high initial depotassiation potential of s-KCO is caused by high stress/strain in the activation process. The difference in curve shape between the first and the second charge curves of s-KCO is attributed to the electrolyte oxidation forming cathode electrolyte interphase (CEI).^{13,48} The depotassiation potential of s-KCO is also lower than that of i-KCO due to fast deintercalation kinetics of s-KCO. These discharge and charge profiles for different cycles exhibit several potential plateaus, which agrees well with the CV results from some reported literatures.^{13,46} Both the CV (Figure 5a) and galvanostatic charge–discharge profiles (Figure S3) show that KCO undergoes multiple phase changes during charge/discharge cycles. In Figure S3, after the first activation cycle the K-ion intercalation process shows that several potential plateaus are separated by sloping curves in the potassium composition range of $0.32 < x < 0.69$ for K_xCoO_2 . Among all, four main plateaus (Nos. 1–4) are related to phase transitions, which consists with previous reports.^{15,47} The existence of potential plateaus indicates formation of some biphasic domains when first-order transitions happen, while the sloping regions are related to single-phase behaviors for solid solution during K-ion intercalation/deintercalation.¹⁵ As shown in Figure 5d, the initial charge and discharge capacities of the s-KCO electrode are 58 and 74 mA h g^{-1} respectively, which are higher than that of the i-KCO electrode. More importantly, the s-KCO electrode maintains a specific capacity of 65 mA h g^{-1} (a retention of $\sim 90\%$) after 100 cycles, which is much higher than that of the i-KCO electrode (27 mA h g^{-1} with a retention of 50% after 100 cycles). The enhanced specific capacity and cycle stability are due to the synergetic effect of the hierarchical structure of the s-KCO.^{6,41,42,44,49}

To further reveal the benefits of the hierarchical structure of s-KCO, the rate performances of the s-KCO and i-KCO cathodes were compared when the currents are increased from 10 to 200 mA g^{-1} (Figure 5e,f, and Figure S4). As can be seen, the s-KCO electrode can deliver an average reversible capacity of 81, 79, 72, 59, and 40 mA h g^{-1} at a current density of 10, 20, 50, 100, and 200 mA g^{-1} , respectively. When the current density is reduced back to 50 mA g^{-1} , a reversible capacity of 71 mA h g^{-1} can be recovered, implying the excellent tolerance for the rapid K-ion intercalation/deintercalation cycles. But for the i-KCO electrode, the specific capacity is dramatically reduced as the current density is increased. At a current density of 100 mA g^{-1} , only 40 mA h g^{-1} can be obtained. Moreover, the s-KCO electrode also exhibits excellent cycling stability. Specifically, a capacity retention of 87% over 300 cycles at a current density of 40 mA g^{-1} is observed (Figure 5g), corresponding to an average capacity loss of 0.04% per cycle. The Coulombic efficiency of the electrode remains $>99\%$ during cycling. In contrast, the capacity of the i-KCO cathode drops quickly with cycling and a

capacity of only 27 mA h g^{-1} is maintained after 100 cycles, corresponding to a low capacity retention of 50% (Figure 5f). In addition, the particle size's effect on the electrochemical performance of i-KCO was also investigated by ball milling of i-KCO for 3 h. As shown in Figure S5, the ball-milled i-KCO exhibits a slightly high initial discharge capacity of 60 mA h g^{-1} , but the capacity decay rate is similar to unmilled i-KCO. Moreover, ball-milled i-KCO also shows a low Coulombic efficiency due to severe side reactions with the electrolyte. The superior potassium storage properties of s-KCO are attributed to uniform hierarchical microsphere structure, in which the primary submicron-sized plates ensure the fast intercalation/deintercalation kinetics by providing a stable K-ion and electron transport pathway. The secondary microsphere structure can effectively buffer the mechanical stress caused by K-ion intercalation/deintercalation and minimize the contact area of the electroactive materials with electrolyte, thus reducing unwanted side reactions and active materials dissolution, leading to a high Coulombic efficiency.^{41,49}

K-ion full batteries based on s-KCO and hard carbon that was derived from rice starch (Figure S6) were fabricated to demonstrate the electrochemical behavior of PIBs, as shown in Figure 6. The hard carbon anode was precycled between 0.01 and 2.0 V (vs K/K⁺) before full cell assembly to remove the large irreversible capacity in the first discharge process shown in Figure S7. The hard carbon has fast charge/discharge rate capability (Figure S8) and long cycling stability (Figure S9), which is best paired with the s-KCO cathode. Figure S10 displays the schematic K-ion full cell configuration with s-KCO as cathode and hard carbon as anode. The potential profiles of s-KCO cathode and hard carbon anode during K-ion insertion/extraction were measured in the half cell with K metal as counter and reference electrode (Figure 6a). Both of the electrode materials were able to achieve reversible potassiation/depotassiation from their respective skeleton structures. Figure 6b presents the charge–discharge profiles of the s-KCO full cell at a current density of 30 mA g^{-1} with cutoff voltages of 3.8 and 0.5 V. The charge/discharge capacities of the second cycle can reach to 73 and 72 mA h g^{-1} , respectively (normalized with the weight of s-KCO). After 50 cycles, the full cell retains a specific capacity of 62 mA h g^{-1} . Besides the large capacity and high retention, the full cell based on s-KCO and hard carbon also exhibits superior rate capability. As shown in Figure 6c, the full cell delivers an average discharge capacity of 71, 65, 56, 43, and 36 mA h g^{-1} at a constant current density of 20, 40, 80, 160, and 320 mA g^{-1} (based on the mass of the cathode), respectively. When the current density is returned to 80 mA g^{-1} , the reversible capacity recovered to 56 mA h g^{-1} , implying the excellent tolerance for the rapid K-ion insertion/extraction cycles. The corresponding charge/discharge curves from current density of 20– 320 mA g^{-1} are presented in Figure 6d. In Figure 6e, the full cell delivers a considerable discharge capacity of 71 mA h g^{-1} with high Coulombic efficiency of $>99\%$ at a current density of 30 mA g^{-1} , and the average Coulombic efficiency is higher than 99% throughout the charge–discharge test. The good capacity retention of $>80\%$ after 100 cycles manifests considerable long-term cycling stability of PIBs based on s-KCO and hard carbon.

The morphology of cycled P2-type $K_{0.6}CoO_2$ electrodes, including s-KCO and i-KCO, were characterized by SEM technique. Figure S11a shows the morphology of s-KCO cathode after the 150th charge/discharge cycle. As it shows, the original morphology of the P2-type $K_{0.6}CoO_2$ microspheres is

well-preserved. As for Figure S11b, the surface of the s-KCO cathode can be found to be covered by a homogeneous passivation layer, which effectively protected the inner s-KCO from reaction with the electrolyte and helped maintain the high electronic conductivity. In contrast, the i-KCO electrode shows a large number of cracks covering the surface with an uneven passivation layer (Figure S11c,d). Apparently, some i-KCO particles were pulverized into smaller pieces. The loss of the active species of i-KCO during charge/discharge cycles resulted in the severe capacity decay in the first 100 cycles, shown in Figure 5d,g. Moreover, the pulverization during potassiation/depotassiation, which exposed new surface to electrolytes, accelerated the side reaction with the electrolyte^{41,44} and increased the contact resistance, resulting in poor electrochemical performance and the structure decay for the i-KCO cathode. Compared with i-KCO, remarkably improved electrochemical performance and structure stability of the s-KCO electrode were observed, which can be attributed to its unique hierarchical structures. The nanoflake $K_{0.6}CoO_2$ primary particles afford a stable K-ion and electron transport pathway, enhancing reaction kinetics and utilization of the active material upon discharge and charge. While the secondary microsphere structure reduces contact area of the active materials with electrolyte, thus reducing unwanted side reactions and active materials dissolution and leading to high Coulombic efficiency.^{41,42,44} Besides, the uniformly formed passivation layer on the surface of the s-KCO cathode further alleviates the side reactions at the interface between microspheres and the electrolyte, resulting in the structural and interfacial stability of the s-KCO electrode. This feature is especially important for the P2-type metal oxides for PIBs, because the side reaction between transition metals and electrolytes usually causes the fast decay of the reversibility.^{11,13,19,42} The above synergetic effect ensures the impressive electrochemical potassium storage performance with high reversible capacity and superior cycling stability of the s-KCO cathode in both half-cell and K-ion full batteries.

In summary, P2-type $K_{0.6}CoO_2$ microspheres were successfully synthesized using a facile and self-templated synthesis method. Benefiting from the special morphology and hierarchical structure, the uniform P2- $K_{0.6}CoO_2$ microspheres provided a high specific capacity of 82 mA h g^{-1} at 10 mA g^{-1} and maintained a high capacity of 65 mA h g^{-1} at 40 mA g^{-1} for over 300 cycles with a capacity decay rate of 0.04% per cycle, which is approximately 5 times lower than the capacity decay rate of layered metal oxides cathodes synthesized by the solid-state method. Meanwhile, the as-synthesized P2- $K_{0.6}CoO_2$ microspheres electrode shows a much better rate capability with a capacity of $>40 \text{ mA h g}^{-1}$ at a current of 200 mA g^{-1} . A full cell with a $K_{0.6}CoO_2$ microspheres cathode and a hard carbon anode further confirms its excellent electrochemical performance by presenting high capacity (71 mA h g^{-1} at 30 mA g^{-1}) and long-term retention ($>80\%$ after 100 cycles). The present self-templated strategy for the synthesis of the hierarchical P2- $K_{0.6}CoO_2$ microspheres can be extended to construct a variety of other layered K-ion cathode materials and should promote the large-scale energy storage applications of PIBs.

■ ASSOCIATED CONTENT

Supporting Information

The Supporting Information is available free of charge on the ACS Publications website at DOI: 10.1021/acs.nanolett.7b05324.

Details of experimental methods, characterizations, electrochemistry, additional figures (Figure S1–S11), additional table (Table S1) (PDF)

■ AUTHOR INFORMATION

Corresponding Author

*E-mail: cswang@umd.edu.

ORCID

Ji Chen: 0000-0003-0326-8304

Xiuquan Zhou: 0000-0002-1361-3880

Chunsheng Wang: 0000-0002-8626-6381

Author Contributions

T.D. and X.F. contributed equally to this work.

Notes

The authors declare no competing financial interest.

■ ACKNOWLEDGMENTS

This work was supported as part of the Nanostructures for Electrical Energy Storage (NEES), an Energy Frontier Research Center funded by the U.S. Department of Energy, Office of Science, Basic Energy Sciences under Award number DESC0001160. We acknowledge the support of the Maryland NanoCenter and its AIM Lab.

■ REFERENCES

- (1) Hassoun, J.; Panero, S.; Reale, P.; Scrosati, B. *Adv. Mater.* **2009**, *21* (47), 4807–10.
- (2) Hu, Y. S.; Demir-Cakan, R.; Titirici, M. M.; Muller, J. O.; Schlogl, R.; Antonietti, M.; Maier, J. *Angew. Chem., Int. Ed.* **2008**, *47* (9), 1645–9.
- (3) Goodenough, J. B.; Park, K. S. *J. Am. Chem. Soc.* **2013**, *135* (4), 1167–76.
- (4) Yoo, H. D.; Shterenberg, I.; Gofer, Y.; Gershinsky, G.; Pour, N.; Aurbach, D. *Energy Environ. Sci.* **2013**, *6* (8), 2265.
- (5) Kim, J. I.; Choi, Y.; Chung, K. Y.; Park, J. H. *Adv. Funct. Mater.* **2017**, *27*, 1701768.
- (6) Han, M. H.; Gonzalo, E.; Singh, G.; Rojo, T. *Energy Environ. Sci.* **2015**, *8* (1), 81–102.
- (7) Luo, C.; Wang, J.; Fan, X.; Zhu, Y.; Han, F.; Suo, L.; Wang, C. *Nano Energy* **2015**, *13*, 537–545.
- (8) Fan, X.; Gao, T.; Luo, C.; Wang, F.; Hu, J.; Wang, C. *Nano Energy* **2017**, *38*, 350–357.
- (9) Fan, X.; Mao, J.; Zhu, Y.; Luo, C.; Suo, L.; Gao, T.; Han, F.; Liou, S.-C.; Wang, C. *Adv. Energy Mater.* **2015**, *5* (18), 1500174.
- (10) Zhu, Y.; Choi, S. H.; Fan, X.; Shin, J.; Ma, Z.; Zachariah, M. R.; Choi, J. W.; Wang, C. *Adv. Energy Mater.* **2017**, *7* (7), 1601578.
- (11) Yabuuchi, N.; Kubota, K.; Dahbi, M.; Komaba, S. *Chem. Rev.* **2014**, *114* (23), 11636–82.
- (12) Yuan, D.; Liang, X.; Wu, L.; Cao, Y.; Ai, X.; Feng, J.; Yang, H. *Adv. Mater.* **2014**, *26* (36), 6301–6.
- (13) Berthelot, R.; Carlier, D.; Delmas, C. *Nat. Mater.* **2011**, *10* (1), 74–80.
- (14) Clément, R. J.; Billaud, J.; Robert Armstrong, A.; Singh, G.; Rojo, T.; Bruce, P. G.; Grey, C. P. *Energy Environ. Sci.* **2016**, *9* (10), 3240–3251.
- (15) Kim, H.; Kim, J. C.; Bo, S.-H.; Shi, T.; Kwon, D.-H.; Ceder, G. *Adv. Energy Mater.* **2017**, *7*, 1700098.
- (16) Ji, B.; Zhang, F.; Song, X.; Tang, Y. *Advanced materials* **2017**, *29*, 19.

- (17) Eftekhari, A. J. *Power Sources* **2003**, *117* (1–2), 249–254.
- (18) Eftekhari, A. J. *Power Sources* **2004**, *126* (1–2), 221–228.
- (19) Eftekhari, A.; Jian, Z.; Ji, X. *ACS Appl. Mater. Interfaces* **2017**, *9* (5), 4404–4419.
- (20) Zhao, J.; Xu, J.; Lee, D. H.; Dimov, N.; Meng, Y. S.; Okada, S. J. *Power Sources* **2014**, *264*, 235–239.
- (21) Bie, X.; Kubota, K.; Hosaka, T.; Chihara, K.; Komaba, S. J. *Mater. Chem. A* **2017**, *5* (9), 4325–4330.
- (22) Xue, L.; Li, Y.; Gao, H.; Zhou, W.; Lu, X.; Kaveevivitchai, W.; Manthiram, A.; Goodenough, J. B. *J. Am. Chem. Soc.* **2017**, *139* (6), 2164–2167.
- (23) Su, D.; McDonagh, A.; Qiao, S. Z.; Wang, G. *Adv. Mater.* **2017**, *29* (1), 1604007.
- (24) Jian, Z.; Hwang, S.; Li, Z.; Hernandez, A. S.; Wang, X.; Xing, Z.; Su, D.; Ji, X. *Adv. Funct. Mater.* **2017**, *27* (26), 1700324.
- (25) Zhang, C.; Xu, Y.; Zhou, M.; Liang, L.; Dong, H.; Wu, M.; Yang, Y.; Lei, Y. *Adv. Funct. Mater.* **2017**, *27* (4), 1604307.
- (26) Tai, Z.; Zhang, Q.; Liu, Y.; Liu, H.; Dou, S. *Carbon* **2017**, *123*, 54–61.
- (27) Luo, W.; Wan, J.; Ozdemir, B.; Bao, W.; Chen, Y.; Dai, J.; Lin, H.; Xu, Y.; Gu, F.; Barone, V.; Hu, L. *Nano Lett.* **2015**, *15* (11), 7671–7.
- (28) He, G.; Nazar, L. F. *ACS Energy Letters* **2017**, *2* (5), 1122–1127.
- (29) Share, K.; Cohn, A. P.; Carter, R.; Rogers, B.; Pint, C. L. *ACS Nano* **2016**, *10*, 9738.
- (30) Kim, H.; Seo, D. H.; Kim, J. C.; Bo, S. H.; Liu, L.; Shi, T.; Ceder, G. *Adv. Mater.* **2017**, *29*, 1702480.
- (31) Wang, X.; Xu, X.; Niu, C.; Meng, J.; Huang, M.; Liu, X.; Liu, Z.; Mai, L. *Nano Lett.* **2017**, *17* (1), 544–550.
- (32) Beltrop, K.; Beuker, S.; Heckmann, A.; Winter, M.; Placke, T. *Energy Environ. Sci.* **2017**, *10*, 2090.
- (33) Jian, Z.; Luo, W.; Ji, X. *J. Am. Chem. Soc.* **2015**, *137* (36), 11566–9.
- (34) Jian, Z.; Xing, Z.; Bommier, C.; Li, Z.; Ji, X. *Adv. Energy Mater.* **2016**, *6* (3), 1501874.
- (35) Komaba, S.; Hasegawa, T.; Dahbi, M.; Kubota, K. *Electrochem. Commun.* **2015**, *60*, 172–175.
- (36) Vaalma, C.; Giffin, G. A.; Buchholz, D.; Passerini, S. *J. Electrochem. Soc.* **2016**, *163* (7), A1295–A1299.
- (37) Wessells, C. D.; Peddada, S. V.; Huggins, R. A.; Cui, Y. *Nano Lett.* **2011**, *11* (12), 5421–5.
- (38) Ling, C.; Chen, J.; Mizuno, F. *J. Phys. Chem. C* **2013**, *117* (41), 21158–21165.
- (39) Mathew, V.; Kim, S.; Kang, J.; Gim, J.; Song, J.; Baboo, J. P.; Park, W.; Ahn, D.; Han, J.; Gu, L.; Wang, Y.; Hu, Y.-S.; Sun, Y.-K.; Kim, J. *NPG Asia Mater.* **2014**, *6* (10), e138.
- (40) Padigi, P.; Thiebes, J.; Swan, M.; Goncher, G.; Evans, D.; Solanki, R. *Electrochim. Acta* **2015**, *166*, 32–39.
- (41) Fang, Y.; Yu, X. Y.; Lou, X. W. D. *Angew. Chem., Int. Ed.* **2017**, *56* (21), 5801–5805.
- (42) Hwang, J. Y.; Oh, S. M.; Myung, S. T.; Chung, K. Y.; Belharouak, I.; Sun, Y. K. *Nat. Commun.* **2015**, *6*, 6865.
- (43) Mao, J.; Fan, X.; Luo, C.; Wang, C. *ACS Appl. Mater. Interfaces* **2016**, *8* (11), 7147–55.
- (44) Fang, Y.; Liu, Q.; Xiao, L.; Ai, X.; Yang, H.; Cao, Y. *ACS Appl. Mater. Interfaces* **2015**, *7* (32), 17977–84.
- (45) Kang, H.; Liu, Y.; Cao, K.; Zhao, Y.; Jiao, L.; Wang, Y.; Yuan, H. *J. Mater. Chem. A* **2015**, *3* (35), 17899–17913.
- (46) Sada, K.; Senthilkumar, B.; Barpanda, P. *Chem. Commun.* **2017**, *53* (61), 8588–8591.
- (47) Pollet, M.; Blangero, M.; Doumerc, J. P.; Decourt, R.; Carlier, D.; Denage, C.; Delmas, C. *Inorg. Chem.* **2009**, *48* (20), 9671–83.
- (48) Yabuuchi, N.; Kajiyama, M.; Iwatate, J.; Nishikawa, H.; Hitomi, S.; Okuyama, R.; Usui, R.; Yamada, Y.; Komaba, S. *Nat. Mater.* **2012**, *11* (6), 512–517.
- (49) Mao, J.; Luo, C.; Gao, T.; Fan, X.; Wang, C. *J. Mater. Chem. A* **2015**, *3* (19), 10378–10385.